Spin Resonance Clock Transition of the Endohedral Fullerene $^{15}N@C_{60}$

R. T. Harding,[1] S. Zhou,[1] J. Zhou,[1] T. Lindvall,[2] W. K. Myers,[3] A. Ardavan,[4] G. A. D. Briggs,[1] K. Porfyrakis,[1] and E. A. Laird[1]

[1]*Department of Materials, University of Oxford, Parks Road, Oxford OX1 3PH, United Kingdom*
[2]*VTT Technical Research Centre of Finland Ltd, Centre for Metrology MIKES, P.O. Box 1000, FI-02044 VTT, Finland*
[3]*Centre for Advanced Electron Spin Resonance, Inorganic Chemistry Laboratory, University of Oxford, South Parks Road, Oxford OX1 3QR, United Kingdom*
[4]*Clarendon Laboratory, Department of Physics, University of Oxford, Parks Road, Oxford OX1 3PU, United Kingdom*

(Received 12 May 2017; published 4 October 2017)

The endohedral fullerene $^{15}N@C_{60}$ has narrow electron paramagnetic resonance lines which have been proposed as the basis for a condensed-matter portable atomic clock. We measure the low-frequency spectrum of this molecule, identifying and characterizing a clock transition at which the frequency becomes insensitive to magnetic field. We infer a linewidth at the clock field of 100 kHz. Using experimental data, we are able to place a bound on the clock's projected frequency stability. We discuss ways to improve the frequency stability to be competitive with existing miniature clocks.

DOI: 10.1103/PhysRevLett.119.140801

Precise and portable frequency references underpin a range of navigation, communication, and sensing infrastructure [1,2]. The most stable references exploit atomic transition frequencies, which are mainly determined by fundamental constants, to minimize the effects of manufacturing variation and of drift [3,4]. The state-of-the-art miniaturized frequency standard is the chip-scale atomic clock (CSAC) [5], which uses optical interrogation of alkali metal vapor [6] confined in a microfabricated vacuum chamber. However, further reductions in size, weight, and power (SWaP) and improved stability are required for broader adoption of portable atomic clocks [7]. Alternative condensed-matter frequency standards, such as V^{++} impurities in MgO [8] or nitrogen vacancy centers in diamond [9], have been proposed to solve these problems, but the necessary stability has not yet been demonstrated. To maximize stability, it is essential to suppress the reference's sensitivity to external perturbations, by, for example, operating at a "clock transition" where the frequency is independent of the magnetic field [10], in addition to employing field shielding and stabilization [3].

Here, we detect and characterize such a "clock transition" in the endohedral fullerene molecule $^{15}N@C_{60}$, demonstrating that it satisfies one criterion for suitability as a frequency reference [3]. This molecule is a promising candidate for a condensed-matter atomic clock [11,12] because of its sharp resonances [13] and the potential for circuit integration using the approach of "1-chip" magnetic resonance [14–16]. Such an atomic clock would lock the frequency of a local oscillator to the reference provided by the spin resonance. We measure the clock transition frequency and field, place an upper limit on the linewidth, measure the signal strength, and set out the requirements to use this molecule as a portable frequency standard.

The endohedral fullerene $^{15}N@C_{60}$ comprises a nitrogen atom encapsulated within a carbon cage [17]. The nitrogen, located at the cage center, retains its ground-state electronic configuration $^4S_{3/2}$ [18], with electron spin $S = 3/2$ and nuclear spin $I = 1/2$. The energy levels of this molecule in a magnetic field $\boldsymbol{B_0} = B_0\hat{z}$ are described by the Hamiltonian

$$\mathcal{H} = g_e\mu_B S_z B_0 - g_N\mu_N I_z B_0 + A\hat{\boldsymbol{S}}\cdot\hat{\boldsymbol{I}}, \tag{1}$$

where g_e (g_N) is the g factor of the electron (nucleus), μ_B (μ_N) is the Bohr (nuclear) magneton, $\hat{\boldsymbol{S}}$ ($\hat{\boldsymbol{I}}$) is the electron (nuclear) spin operator, and A is the isotropic hyperfine constant [13]. Zero-field splitting is neglected due to the near-spherical symmetry of the system [19].

Figure 1(a) shows simulated energy eigenstates of the Hamiltonian (1) as a function of magnetic field. The simulation parameters are $g_e = 2.00204$ and $|A|/h = 22.35$ MHz [20], with $g_N = -0.566$ [21,22]. The negative nuclear g factor leads to a negative value of A, leading to an inverted energy level manifold [3]. Near zero field, the eigenstates form a pair of hyperfine-split multiplets labeled by quantum numbers $|F, m_F\rangle$, where $\hat{\boldsymbol{F}} = \hat{\boldsymbol{I}} + \hat{\boldsymbol{S}}$. At high fields, where the Zeeman interaction dominates, the level diagram simplifies to four doublets labeled by $|m_S, m_I\rangle$. Between these limits lies a crossover region in which the eigenstates are mixed in either basis.

In a magnetic resonance experiment, the allowed transitions between energy levels depend on the orientation of the oscillating drive field $\boldsymbol{B}_1$ relative to $\boldsymbol{B}_0$. The transition frequencies are plotted in Figs. 1(c) and 1(d) for perpendicular mode ($\boldsymbol{B}_1 \perp \boldsymbol{B}_0$) and parallel mode ($\boldsymbol{B}_1 \| \boldsymbol{B}_0$), respectively. To indicate the strength of each transition, traces are colored according to the magnitude of the transition matrix element $\langle f|g_e S_{x(z)} + g_N I_{x(z)}|i\rangle$ for

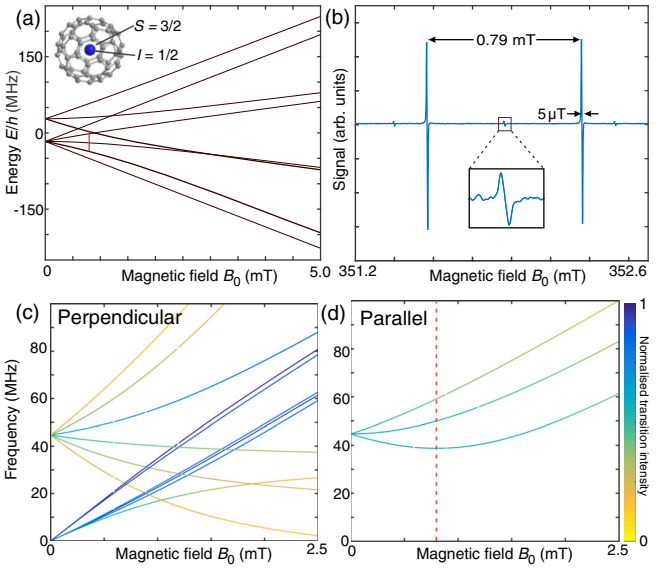

FIG. 1. (a) Simulated energy levels of $^{15}N@C_{60}$ as a function of magnetic field. The clock transition is denoted by a vertical red line. Inset: molecular structure, labeled with electron (S) and nuclear (I) spins. (b) EPR spectrum of $^{15}N@C_{60}$ measured at the X band ($f = 9.86$ GHz). The zoom in highlights the contribution of residual $^{14}N@C_{60}$. (c),(d) Simulated frequencies of allowed transitions for the driving magnetic field applied perpendicular (c) and parallel (d) to the static magnetic field B_0. Traces are colored according to transition intensity. The clock field is marked with a dashed line.

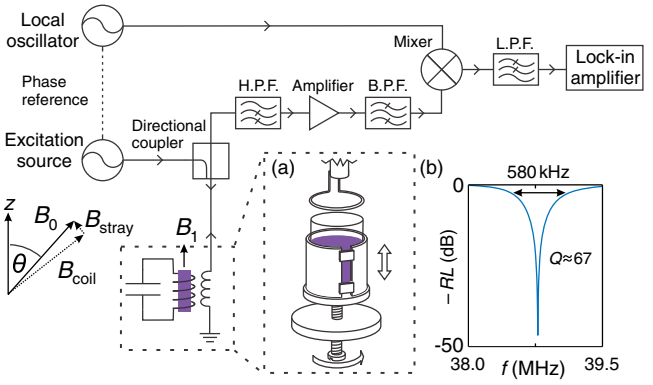

FIG. 2. Measurement setup. An excitation source and local oscillator are implemented using two phase-locked synthesisers. The signal reflected from the resonator is high-pass filtered (H. P. F.) before amplification in order to suppress inductive pickup of the modulation field. The signal is subsequently band-pass filtered (B. P. F.) and mixed down to baseband, before being low-pass filtered (L. P. F.) and measured using a lock-in amplifier synchronized with the modulation field. Inset (a): Loop-gap resonator with sample (purple). Adjustable coupling between the antenna and resonator is achieved by mechanical displacement of the resonator (vertical block arrow) via a screw-thread mechanism. Inset (b): Reflection from the resonator, demonstrating near-critical coupling and good return loss (RL) for maximum sensitivity. For this particular resonator, $Q \approx 67$.

perpendicular- (parallel-) mode transitions between the initial state $|i\rangle$ and final state $|f\rangle$.

The clock transition occurs at an anticrossing between two levels that are mixed by the hyperfine interaction [Fig. 1(a)]. At the clock field, the transition frequency is insensitive to magnetic field ($df/dB = 0$). This transition can be driven in parallel mode [Fig. 1(d)] and occurs at a field $B_{\text{clock}} = |A|/(g_e\mu_B + g_N\mu_N) \approx 0.8$ mT with a frequency $f_{\text{clock}} = \sqrt{3}|A|/h \approx 39$ MHz.

A $^{15}N@C_{60}$ sample was prepared by ion implantation of C_{60} using $^{15}N_2$ (isotopic purity 98%) [17]. The crude sample was dissolved in toluene and purified by a high-performance liquid chromatography method to a purity ($^{15}N@C_{60}$:C_{60}) of ~6000 ppm [23]. The sample was characterized at the X band [Fig. 1(b)], showing a pair of narrow spin resonances as expected from the hyperfine interaction in $^{15}N@C_{60}$ [17]. For low-field experiments, the sample was redissolved in deoxygenated CS_2 under N_2 atmosphere (<0.01 ppm O_2) [24] and flame sealed in a Suprasil tube. The spin number is $N_{\text{spin}} \approx 1.4 \times 10^{16}$ in a volume 0.55 cm^3.

To characterize the clock transition, we performed fixed-frequency swept-field continuous-wave spin resonance measurements using the circuit of Fig. 2. A swept magnetic field $\boldsymbol{B}_{\text{coil}}$ was generated using a Helmholtz electromagnet oriented for either perpendicular- or parallel-mode operation. Small stray magnetic fields $\boldsymbol{B}_{\text{stray}}$ slightly shift $\boldsymbol{B}_0$ away from the nominal value set by $\boldsymbol{B}_{\text{coil}}$. To obtain each spectrum, the sample was loaded into one of a series of interchangeable loop-gap resonators (LGRs) [25] spanning the range 38–70 MHz. The frequency of each LGR was adjusted using capacitors soldered across the gap [26].

Spin resonance was detected by monitoring the sample-loaded resonator's radio-frequency (rf) reflection coefficient as a function of the magnetic field [27,28]. The LGR was probed via a coupling antenna, with the separation adjusted mechanically to achieve near-critical coupling (return loss RL > 50 dB and loaded quality factor $Q \sim 70$). A rf excitation with power $P = -21$ dBm was applied to the LGR via a directional coupler. The oscillating magnetic field $\boldsymbol{B}_1$ generated by the rf excitation, with frequency f, is linearly polarized along the axis of the LGR. Near the clock field, with $f \approx f_{\text{clock}}$, its amplitude $B_1 \approx \sqrt{[(\mu_0 PQ)/2\pi Vf]} \approx 1.9\mu$T, where μ_0 is the permeability of free space, and the resonator volume $V \approx 0.8$ cm^3.

The reflected signal was filtered and amplified before being mixed with the local oscillator signal to generate a homodyne voltage. The phase between the local oscillator and the excitation source was chosen to maximize the dc component of this voltage, which maximizes sensitivity to the amplitude of the reflected signal. The excitation frequency was set 3 kHz above the LGR frequency to suppress the effects of drift in the coupling [29]. For improved sensitivity, a small modulation field with amplitude $B_{\text{mod}} \approx 1.1 \times 10^{-5}$ T was applied parallel to $\boldsymbol{B}_0$ at a frequency $f_{\text{mod}} \approx 5$ kHz, allowing the homodyne voltage to

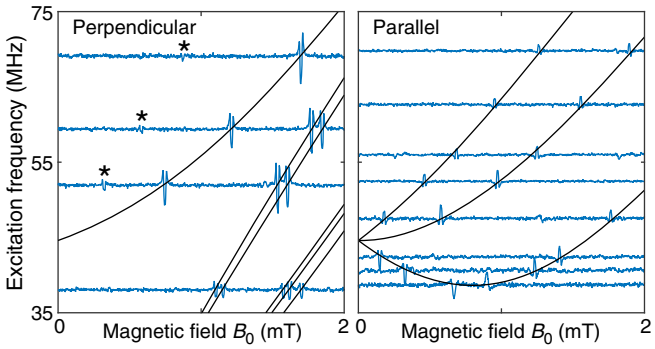

FIG. 3. Perpendicular- and parallel-mode EPR spectra of $^{15}N@C_{60}$. Blue: lock-in signal (arbitrary units) as a function of rescaled magnetic field B_0, offset such that the baseline of each trace aligns with the corresponding excitation frequency. Each trace is an average of up to 100 sweeps. Black: fit to resonant fields using exact solutions to the Hamiltonian given in Eq. (1). In perpendicular mode, it is possible to observe resonances (marked by filled star) that were not fitted due to a low signal-to-noise ratio.

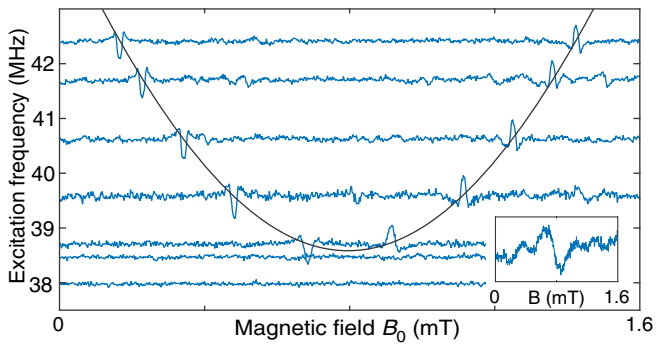

FIG. 4. Parallel-mode EPR spectra of the clock transition near the clock field. Blue: lock-in signal (arbitrary units) as a function of the rescaled magnetic field at selected frequencies. Black line: fit to resonant fields. Inset: spectrum measured at 38.474 MHz, cutting near the tip of the parabola. A larger modulation amplitude was necessary to detect the nearly field-independent transition.

be detected using a lock-in amplifier synchronized with this modulation.

Low-field EPR spectra, shown in Fig. 3, match well the predictions of Figs. 1(c) and 1(d). The resonant fields are extracted by fitting the peaks with the second derivative of a Lorentzian. For quantitative analysis, we then fit these resonant fields using the energy levels derived from Eq. (1) [30]. We account for small differences between the nominal field B_{coil} and the true field B_0 at the sample by fitting the data using $B_0 = \alpha B_{\mathrm{coil}} + B_{\mathrm{offset}}$, where α is a correction parameter, reflecting sample misalignment and uncertainty in the calculated coil constant, and B_{offset} is an environmental offset field. Fitting parallel and perpendicular data sets simultaneously, while fixing $g_e = 2.00204$ and $g_N = -0.566$, we extract $|A|/h = 22.30 \pm 0.02$ MHz, $\alpha = 1.024 \pm 0.003$, and $B_{\mathrm{offset}} = -28 \pm 4$ μT, where error bars are one standard deviation intervals derived from the fits. The spectra are plotted in terms of B_0 rather than B_{coil}.

Figure 4 shows the parallel-mode spectra used to characterize the clock transition. Fitting these data as in Fig. 3, we extract $|A|/h = 22.277 \pm 0.001$ MHz, $\alpha = 1.0257 \pm 0.0005$, and $B_{\mathrm{offset}} = -12.1 \pm 0.5$ μT. The value of A is consistent between Fig. 3 and Fig. 4 and lies within the range of previous X-band measurements [20,31]. The values obtained for B_{offset} are much smaller than B_{coil} and are consistent with the geomagnetic field.

Measuring near the clock field reduces the sensitivity of the transition frequency to magnetic field fluctuations. To quantify this, we extract field-domain linewidths δB from the spectra of Fig. 4 [30]. As a function of the deviation from the clock field $\Delta B_C = |B_0 - B_{\mathrm{clock}}|$, the field-domain linewidth δB increases towards the clock field (Fig. 5). However, when this field linewidth is converted to a frequency-domain linewidth $\delta f = |(df)/dB_0|\delta B$, the resonance sharpens toward the clock transition as expected. Although our field-swept configuration precludes directly measuring the linewidth at the clock field, we estimate the corresponding dephasing time T_2^* by assuming that an intrinsic linewidth set by T_2^* adds in quadrature with broadening due to magnetic field fluctuations of strength B_{var}

$$[\delta f(\Delta B_C)]^2 = \left(\frac{1}{\pi T_2^*}\right)^2 + \left(\frac{df(\Delta B_C)}{dB} B_{\mathrm{var}}\right)^2. \quad (2)$$

Here, B_{var} accounts for line broadening due to both the modulation field and environmental field noise. Fitting this model (Fig. 5) gives $T_2^* = 3.0 \pm 0.4$ μs and $B_{\mathrm{var}} = 26.2 \pm 0.9$ μT, including the contribution of the modulation field.

These measurements enable an assessment of the feasibility of an endohedral fullerene frequency standard. The Allan deviation $\sigma_y(\tau)$, which parameterizes [32] the fractional frequency stability over time τ, is [4]

$$\sigma_y(\tau) \approx \frac{1}{\mathrm{SNR} Q_A} \sqrt{\frac{1}{\tau}}, \quad (3)$$

for short measurement times τ such that the noise spectrum is approximately white. Here, SNR and Q_A are the signal-to-noise ratio and quality factor of the clock transition resonance signal respectively. The signal-to-noise ratio $\mathrm{SNR} = S_0/\delta S$, where S_0 is the signal amplitude, and δS is the root-mean-square noise per $\sqrt{\mathrm{Hz}}$ bandwidth; the transition quality factor $Q_A = f_{\mathrm{clock}}/\delta f$. Using the measured values of signal amplitude $S_0 \approx 5$ nV, input-referred noise voltage $\delta S \approx 2.5$ nV Hz$^{-1/2}$, clock frequency $f_{\mathrm{clock}} = \sqrt{3}|A| \approx 38.6$ MHz, and linewidth $\delta f \approx 100$ kHz; Eq. (3) predicts $\sigma_y \approx 1.3 \times 10^{-3}\ \tau^{-1/2}$, where the numerical prefactor has units $s^{1/2}$, such that σ_y is dimensionless.

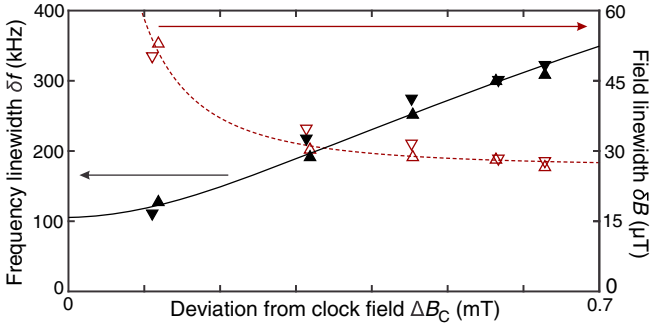

FIG. 5. Linewidth as a function of deviation from the clock field. Left axis: frequency-domain linewidth δf above (filled up triangle) and below (filled down triangle) the clock field. Right axis: field-domain linewidth δB above (up triangle) and below (down triangle) the clock field. Solid black line: fit to the frequency-domain linewidth generated using Eq. (2). Dashed red line: the same fit mapped to the field domain. Arrows indicate the relevant axes for the fits.

To improve the performance, it will be necessary to optimize SNR and Q_A. Improvements to the signal strength would come from increased spin density, achieved by using higher-purity material and by choosing a solvent that allows for a higher molecular concentration or even a powder sample. The SNR could also be improved by reducing electronic noise. To increase Q_A, the linewidth should be reduced below our measured value, the origin of which is currently unknown. For comparison, coherence time $T_2 = 80\ \mu$s was attained in a carefully prepared ^{14}N@C$_{60}$ sample measured at the X band [13], a significant improvement over the T_2^* value measured here. There are other molecular species with clock transitions at higher frequencies [33], but these do not benefit from the fullerene cage to protect the spin states from environmental decoherence.

We now consider what would be necessary to make an endohedral fullerene clock competitive with existing miniature atomic clocks, which achieve [34] short-term Allan deviations $\sigma_y \leq 3 \times 10^{-10}$ for $\tau = 1$ s (Table I). Firstly, we consider how to increase the SNR. Our spin density ($n \approx 2.5 \times 10^{22}$ m^{-3}) approaches the limit set by the saturation concentration of C$_{60}$ in CS$_2$ (7.9 mg ml^{-1}) [35] given the sample purity. Using pure material would increase the signal by a factor of 170, while using 1-chloronaphthalene solvent (saturation concentration 51 mg ml^{-1}) would permit an additional factor of 10. The LGR could be replaced by a solenoid with a similar filling factor and improved rf quality factor $Q \approx 200$ [36], giving a roughly threefold increase in signal. Furthermore, there is scope to reduce voltage noise from $\delta S \approx 2.5$ nV Hz$^{-1/2}$ to the room-temperature Johnson-Nyquist limit $\delta S \approx 0.9$ nV Hz$^{-1/2}$. Combining these improvements multiplicatively would lead to a short-term Allan deviation $\sigma_y \sim 1 \times 10^{-7}\ \tau^{-1/2}$ given our measured linewidth.

Secondly, we consider improvements in linewidth at the clock transition. If the linewidth could be reduced to $\delta f \sim 100$ Hz, a demanding requirement, the Allan deviation would be $\sigma_y \sim 1 \times 10^{-10}\ \tau^{-1/2}$. Alternatively, using a powder sample ($n \approx 1.4 \times 10^{27}$ m^{-3}) instead of a solution would allow the same performance to be achieved with the larger linewidth $\delta f \sim 4$ kHz. However, in both powder and high-density solutions, it is critical that dipolar coupling does not broaden these linewidths. Such broadening is typically suppressed at the clock field [10,33].

TABLE I. Summary of potential improvement factors such that a ^{15}N@C$_{60}$-based frequency standard could achieve a short-term Allan deviation $\sigma_y(\tau = 1\ \text{s}) \sim 1 \times 10^{-10}$.

Limiting factor	Change	Relative improvement
Purity (%)	0.6 → 100	170
Concentration (mg ml^{-1})	5 → 51	10
Resonator Q factor	70 → 200	2.9
Electronic noise (nV Hz$^{-1/2}$)	2.5 → 0.9	2.8
Linewidth (Hz)	$10^5 \rightarrow 10^2$	1000
	Product	1.4×10^7

For large τ, $\sigma_y(\tau)$ is greater than the prediction of Eq. (3) because of drifts in the clock parameters. For example, thermal drift enters via the temperature dependence of the hyperfine constant [37], known from ^{14}N@C$_{60}$ measurements to be $(1/A)[(dA)/dT] = 89$ ppm/K. The development of a stable frequency standard will therefore require thermal isolation, temperature stabilization, or compensation. Thermistors have insufficient long-term stability to permit stable clock operation [9]. However, suitable temperature monitoring could be achieved by measuring simultaneously three transitions, which together allow errors in frequency, magnetic field, and temperature to be extracted.

As a route to improving both short- and long-term stability, the endohedral fullerene ^{31}P@C$_{60}$, with the same spin quantum numbers as ^{15}N@C$_{60}$ but larger hyperfine coupling ($A \approx 138$ MHz [38]), offers a clock frequency $f_{\text{clock}} \approx 240$ MHz. Given a linewidth $\delta f \approx 350$ kHz [38], the predicted transition quality factor $Q_A \approx 700$ for ^{31}P@C$_{60}$ compares favorably to the measured value $Q_A \approx 400$ for ^{15}N@C$_{60}$. The ^{31}P@C$_{60}$-based frequency standard would also benefit from an approximately twentyfold improvement due to the frequency-dependent SNR scaling, where SNR $\propto f_{\text{clock}}^{7/4}$ [36]. Assuming the same sample volume, concentration, and purity as considered above, the improved SNR and Q_A would lead to a fortyfold improvement of the predicted short-term Allan deviation relative to that of a ^{15}N@C$_{60}$-based standard, such that $\sigma_y \sim 3 \times 10^{-9}\ \tau^{-1/2}$ might be achieved in solution without further improvements in linewidth. To achieve $\sigma_y \sim 1 \times 10^{-10}\ \tau^{-1/2}$ would require a linewidth $\delta f \sim 10$ kHz. Furthermore, ^{31}P@C$_{60}$ exhibits a weaker temperature dependence $(1/A)[(dA)/dT] = 74$ ppm/K [37].

We have demonstrated that $^{15}N@C_{60}$ possesses a spin resonance clock transition and therefore fulfils one of the requirements for a condensed matter atomic clock. This is the first observation of a clock transition in a molecular system at room temperature. Other requirements are a reproducible transition frequency, a sharp resonance, and high SNR. The molecular nature of endohedral fullerenes is favorable for reproducibility, while the requirements for sharpness and SNR are addressed in Table I. The data presented here do not yet demonstrate clock operation, which would require a swept-frequency measurement at the clock field. Furthermore, useful operation will require purer material and a much narrower linewidth. The latter requirement is particularly stringent, because the condensed-matter environment introduces spin relaxation mechanisms that will limit the minimum achievable linewidth at the clock transition [13]. Combined with a lower frequency clock transition than in alkali metals, due to the weak hyperfine coupling of $^{15}N@C_{60}$, the maximum Q_A will likely be less than is achieved in vapor-based clocks. To compensate for this, it will be necessary to improve the SNR of the spin resonance signal. However, our approach would eliminate the complexity of vapor-based clocks in favor of a single radio-frequency circuit. This would enable further miniaturization, robustness, and ease of manufacture, leading to a wider range of application of atomic clocks.

We thank J. Liu, J. F. Gregg, P. Dallas, and C. J. Wedge for useful discussions, and J. J. Le Roy for assistance with sample preparation. We acknowledge DSTL, EPSRC (EP/J015067/1, EP/K030108/1, EP/N014995/1, EP/P511377/1), the Royal Academy of Engineering, a Marie Curie CIG award, and LocatorX Inc. of Jackson Beach, Florida.

[1] J. R. Vig, Military applications of high accuracy frequency standards and clocks, IEEE Trans. Ultrason. Ferroelectr. Freq. Control **40**, 522 (1993).
[2] A. M. Shkel, Precision navigation and timing enabled by microtechnology: Are we there yet? in *2010 IEEE Sensors* (IEEE, New York, USA, 2010) pp. 5–9.
[3] J. Vanier and C. Audoin, *The Quantum Physics of Atomic Frequency Standards* (A. Hilger, Philadelphia, USA, 1989).
[4] F. Riehle, *Frequency standards: Basics and Applications* (WILEY-VCH Verlag GmbH & Co. KGaA, Weinheim, Germany, 2004).
[5] S. Knappe, V. Shah, P. D. D. Schwindt, L. Hollberg, J. Kitching, L.-A. Liew, and J. Moreland, A microfabricated atomic clock, Appl. Phys. Lett. **85**, 1460 (2004).
[6] N. Cyr, M. Tetu, and M. Breton, All-optical microwave frequency standard: a proposal, IEEE Trans. Instrum. Meas. **42**, 640 (1993).
[7] R. Lutwak, A. Rashed, M. Varghese, G. Tepolt, J. LeBlanc, M. Mescher, D. K. Serkland, K. M. Geib, G. M. Peake, and S. Römisch, The chip-scale atomic clock—prototype evaluation, in *Proceedings of the 39th Annual Precise Time and Time Interval Systems and Applications Meeting* (Institute of Navigation, Manassas, USA, 2007) pp. 269–290.
[8] C. J. White and A. Hajimiri, A solid-state atomic frequency standard, Proc. IEEE Internat. Freq. Control Symp. Exp. **2005**, 940 (2005).
[9] J. S. Hodges, N. Y. Yao, D. Maclaurin, C. Rastogi, M. D. Lukin, and D. Englund, Timekeeping with electron spin states in diamond, Phys. Rev. A **87**, 032118 (2013).
[10] G. Wolfowicz, A. M. Tyryshkin, R. E. George, H. Riemann, N. V. Abrosimov, P. Becker, H.-J. Pohl, M. L. W. Thewalt, S. A. Lyon, and J. J. L. Morton, Atomic clock transitions in silicon-based spin qubits, Nat. Nanotechnol. **8**, 561 (2013).
[11] E. C. Hannah and M. A. Brown, Conceptual design of a micron-scale atomic clock, arXiv:0707.4624.
[12] G. A. D. Briggs and A. Ardavan, US Patent No. 8, 217, 724 (2012).
[13] J. J. L. Morton, A. M. Tyryshkin, A. Ardavan, K. Porfyrakis, S. A. Lyon, and G. A. D. Briggs, Electron spin relaxation of $N@C_{60}$ in CS_2, J. Chem. Phys. **124**, 014508 (2006).
[14] N. Sun, T. J. Yoon, H. Lee, W. Andress, R. Weissleder, and D. Ham, Palm NMR and 1-chip NMR, IEEE J. Solid-State Circuits **46**, 342 (2011).
[15] J. Anders, J. Handwerker, M. Ortmanns, and G. Boero, A low-power high-sensitivity single-chip receiver for NMR microscopy, J. Magn. Reson. **266**, 41 (2016).
[16] M. Grisi, G. Gualco, and G. Boero, A broadband single-chip transceiver for multi-nuclear NMR probes, Rev. Sci. Instrum. **86**, 044703 (2015).
[17] T. Almeida Murphy, Th. Pawlik, A. Weidinger, M. Höhne, R. Alcala, and J.-M. Spaeth, Observation of Atomlike Nitrogen in Nitrogen-Implanted Solid C_{60}, Phys. Rev. Lett. **77**, 1075 (1996).
[18] K. Lips, M. Waiblinger, B. Pietzak, and A. Weidinger, Atomic nitrogen encapsulated in fullerenes: Realization of a chemical Faraday cage, Phys. Status Solidi (a) **177**, 81 (2000).
[19] G. W. Morley, Ph.D. thesis, University of Oxford, 2005.
[20] B. Pietzak, M. Waiblinger, T. Almeida Murphy, A. Weidinger, M. Höhne, E. Dietel, and A. Hirsch, Properties of endohedral $N@C_{60}$, Carbon **36**, 613 (1998).
[21] J. D. Baldeschwieler, Double resonance spectra of N^{14} and N^{15} ammonium ion, J. Chem. Phys. **36**, 152 (1962).
[22] N. J. Stone, Table of nuclear magnetic dipole and electric quadrupole moments, At. Data Nucl. Data Tables **90**, 75 (2005).
[23] M. Kanai, K. Porfyrakis, G. A. D. Briggs, and T. J. S. Dennis, Purification by HPLC and the UV/Vis absorption spectra of the nitrogen-containing *incar*-fullerenes $i NC_{60}$, and $i NC_{70}$, Chem. Commun. (Cambridge) **0**, 210 (2004).
[24] J. J. L. Morton, A. M. Tyryshkin, A. Ardavan, K. Porfyrakis, S. A. Lyon, and G. A. D. Briggs, Environmental effects on electron spin relaxation in $N@C_{60}$, Phys. Rev. B **76**, 085418 (2007).
[25] W. Froncisz and J. S. Hyde, The loop-gap resonator: A new microwave lumped circuit ESR sample structure, J. Magn. Reson. (1969) **47**, 515 (1982).
[26] 0505C series nonmagnetic high-Q, low-ESR (NP0 TC) capacitors, Passive Plus, Inc., New York, USA.
[27] C. A. Whitmer, R. T. Weidner, J. S. Hsiang, and P. R. Weiss, Magnetic resonance absorption in the chrome alums, Phys. Rev. **74**, 1478 (1948).

[28] C. P. Slichter, *Principles of Magnetic Resonance*, (Springer-Verlag, Berlin, Germany, 1990), 3rd ed.
[29] C. P. Poole, *Electron Spin Resonance: A Comprehensive Treatise on Experimental Techniques* (Wiley-Interscience, New York, USA, 1983), 2nd ed.
[30] See Supplemental Material at http://link.aps.org/supplemental/10.1103/PhysRevLett.119.140801 for a derivation of the observed lineshape and fitting procedures.
[31] W. Harneit, C. Meyer, A. Weidinger, D. Suter, and J. Twamley, Architectures for a spin quantum computer based on endohedral fullerenes, Phys. Status Solidi (b) **233**, 453 (2002).
[32] D. W. Allan, Time and frequency (time-domain) characterization, estimation, and prediction of precision clocks and oscillators, IEEE Trans. Ultrason. Ferroelectr. Freq. Control **34**, 647 (1987).
[33] M. Shiddiq, D. Komijani, Y. Duan, A. Gaita-Ariño, E. Coronado, and S. Hill, Enhancing coherence in molecular spin qubits via atomic clock transitions, Nature (London) **531**, 348 (2016).
[34] Quantum^{TM} SA.45s CSAC chip scale atomic clock, Microsemi Corporation, Aliso Viejo, California, USA (2017).
[35] R. S. Ruoff, D. S. Tse, R. Malhotra, and D. C. Lorents, Solubility of fullerene C_{60} in a variety of solvents, J. Phys. Chem. **97**, 3379 (1993).
[36] D. I. Hoult and R. E. Richards, The signal-to-noise ratio of the nuclear magnetic resonance experiment, J. Magn. Reson. (1969) **24**, 71 (1976).
[37] B. Pietzak, A. Weidinger, K.-P. Dinse, and A. Hirsch, Group V Endohedral Fullerenes: N@C_{60}, N@C_{70}, and P@C_{60}, in *Endofullerenes: A New Family of Carbon Clusters*, (Springer, Netherlands, 2002) 1st ed., Vol. 3, Chap. 2.
[38] C. Knapp, N. Weiden, H. Kass, K.-P. Dinse, B. Pietzak, M. Waiblinger, and A. Weidinger, Electron paramagnetic resonance study of atomic phosphorus encapsulated in [60] fullerene, Mol. Phys. **95**, 999 (1998).

SUPPLEMENTARY MATERIAL

The spin resonance clock transition of the endohedral fullerene $^{15}N@C_{60}$

R.T. Harding,[1] S. Zhou,[1] J. Zhou,[1] T. Lindvall,[2] W. K. Myers,[3]
A. Ardavan,[4] G.A.D. Briggs,[1] K. Porfyrakis,[1] and E.A. Laird[1]

[1] *Department of Materials, University of Oxford, Parks Road, Oxford OX1 3PH, United Kingdom*
[2] *VTT Technical Research Centre of Finland Ltd, Centre for Metrology MIKES, P.O. Box 1000, FI-02044 VTT, Finland*
[3] *Centre for Advanced Electron Spin Resonance, Inorganic Chemistry Laboratory, University of Oxford, South Parks Road, Oxford OX1 3QR, United Kingdom*
[4] *Clarendon Laboratory, Department of Physics, University of Oxford, Parks Road, Oxford OX1 3PU, United Kingdom*

(Dated: August 21, 2017)

I. LINESHAPE

Here, we derive the lineshape used to fit the resonances displayed in Figure 3 and Figure 4 of the main text, which differs from the lineshape typically observed in continuous-wave electron paramagnetic resonance (EPR) experiments. In most EPR experiments, the spectrometer is adjusted to maximise sensitivity to the absorption of radiation in the spin ensemble rather than its effect on the phase of radiation reflected from the resonator. This is achieved by using automatic frequency control (AFC) to lock the frequency of the excitation to that of the resonator, and selecting a suitable local oscillator phase, in order to suppress the response due to the component of magnetic susceptibility that corresponds to phase shifts. When used in conjunction with field- or frequency-modulation and lock-in detection, the observed signals are therefore described by the first derivative of an absorption lineshape, as shown in Figure 1(b) of the main text.

In contrast, the signals displayed in Figure 3 and Figure 4 are well fitted by the second derivative of a Lorentzian. This second-derivative lineshape is typical for signals due to the phase component observed using lock-in detection. In this experiment, the spectrometer is sensitive to the phase response of the spin ensemble despite the phase of the local oscillator being chosen to maximise sensitivity to changes in amplitude of radiation reflected from the LGR. This is because the excitation frequency was slightly detuned from the cavity resonant frequency and, in the absence of AFC, the shift in the resonator frequency caused by the spin ensemble is converted to an amplitude signal by the slope of the resonator dip.

To understand this phenomenon quantitatively, we consider the effect of the spin ensemble on the LGR resonant frequency ω_{res}. The LGR is modelled using the circuit displayed in Figure S1, which comprises an inductance L, capacitance C, and a resistance R that models losses in the circuit. The inductance of the bare resonator

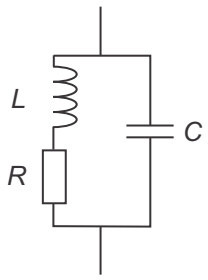

FIG. S1. Lumped element model of loop gap resonator, comprising inductance L (loop), capacitance C, and resistance R.

is perturbed by the magnetic susceptibility of the sample

$$\chi = \chi' - i\chi'', \tag{S1}$$

such that the resonator inductance is given by

$$L = L_0\left[1 + \eta\chi' - i\eta\chi''\right], \tag{S2}$$

where the inductance of the bare loop is given by L_0 and the filling factor η parameterises the overlap between the sample and the oscillating magnetic field of amplitude B_1 and angular frequency ω [S1]. By considering the impedance

$$Z = \left[i\omega C + \frac{1}{i\omega L + R}\right]^{-1} \tag{S3}$$

of the resonant circuit, and by treating the effect of the sample magnetic susceptibility as a perturbation, such that $\eta\chi(\omega) \ll 1$, one can derive the expression

$$\omega_{\mathrm{res}} = \omega_0\left[1 - \frac{1}{2}\eta\chi'\right], \tag{S4}$$

where

$$\omega_0 = \frac{1}{\sqrt{L_0 C}}\left(1 - \frac{CR^2}{2L}\right) \tag{S5}$$

is the resonant frequency of the bare resonator. These calculations assume that the quality factor of the resonator $Q \gg 1$.

In the absence of saturation, the value of χ' is given by

$$\chi'(\omega_{\rm spin}, \omega_{\rm rad}) = \overline{\chi}(\omega_{\rm spin}) \frac{(\omega_{\rm spin} - \omega_{\rm rad})}{(\delta\omega/2)^2 + (\omega_{\rm rad} - \omega_{\rm spin})^2}, \tag{S6}$$

where $\omega_{\rm spin}$ is the resonant frequency of the spin ensemble at a field B_0, $\omega_{\rm rad}$ is the frequency of applied radiation, and $\delta\omega$ is the width of the resonance in the angular frequency domain for a given value of $\omega_{\rm rad}$. The quantity $\overline{\chi}$, with dimension s^{-1}, parameterises the magnitude of the magnetic susceptibility for a given energy splitting between the clock states.

In general, $\omega_{\rm spin}$ is a non-linear function of magnetic field B_0; however, over the small range of magnetic field where the ensemble is near resonance ($\omega_{\rm spin} \approx \omega_{\rm rad}$), we can approximate it as a linear function such that $\omega_{\rm spin} - \omega_{\rm rad} = \gamma_{\rm eff}\Delta B$, where $\gamma_{\rm eff}$ is the effective gyromagnetic ratio at the predicted resonant field $B_{\rm rad}$ for which $\omega_{\rm spin} = \omega_{\rm rad}$, and $\Delta B = B_0 - B_{\rm rad}$. Furthermore, we take the susceptibility parameter $\overline{\chi}$ as constant over one linewidth, such that $\overline{\chi}(\omega_{\rm spin}) \approx \overline{\chi}(\omega_{\rm rad})$. In this case, Equation (S6) reduces to

$$\chi'(\Delta B, \omega_{\rm rad}) = \frac{\overline{\chi}(\omega_{\rm rad})}{\gamma_{\rm eff}} \cdot \frac{(\Delta B)}{(\delta B/2)^2 + (\Delta B)^2}, \tag{S7}$$

where the field domain linewidth $\delta B = \delta\omega/\gamma_{\rm eff}$. Substituting Equation (S7) into Equation (S4), we can see that the frequency shift $\Delta\omega_{\rm res}$ of the resonator is given by the derivative of a Lorentzian in the field domain. For small cavity frequency shifts, the reflection of the detuned excitation radiation is linearly converted into an amplitude signal by the frequency-dependent reflection coefficient of the resonator. The reflected signal amplitude is therefore described by a Lorentzian-derivative lineshape $S \propto \chi'(\Delta B, \omega_{\rm rad})$, and hence the observed signal after field modulation and phase-sensitive detection

$$S_{\rm obs} = k \frac{\partial}{\partial(\Delta B)} \left[\chi'(\Delta B, \omega_{\rm rad}) \right] \tag{S8}$$

is described the second-derivative of a Lorentzian in the field domain. The experimental parameter k parameterises the spectrometer's sensitivity. The resonance signals in each fixed-frequency, swept-field spectrum are fitted using an equation whose functional form is given by Equation (S8), with the addition of a dc offset due to, for example, inductive pickup of the modulation field. The fit parameters are signal amplitude S_0, field domain linewidth δB, resonant field $B_{\rm res}$, and dc offset.

II. FITTING THE RESONANCE LOCATIONS

To fit the data shown in Figure 3 and Figure 4 of the main text, the spin Hamiltonian was diagonalised to give analytic expressions for the energy eigenlevels $E_1(B_0) \ldots E_8(B_0)$ as a function of magnetic field B_0. From these expressions, we calculate the transition frequencies $f_1 \ldots f_N$ as a function of magnetic field. The set of resonant fields derived from the fits described in Section I was divided into subsets i, each corresponding to a particular allowed transition frequency $f_i = f_i(B_0, A, g_{\rm e}, g_{\rm N})$.

We find it necessary to account for small differences between the nominal field $B_{\rm coil}$ generated by the Helmholtz coil and the true field B_0 at the sample by fitting the data using $B_0 = \alpha B_{\rm coil} + B_{\rm offset}$, where α is a correction parameter, reflecting sample misalignment and uncertainty in the calculated coil constant, and $B_{\rm offset}$ is an environmental offset field. Therefore, we fit the set of resonant fields for transition i at a given transition frequency using the relationship $f_i = f_i(B_{\rm coil}, B_{\rm offset}, \alpha, A, g_{\rm e}, g_{\rm N})$, using $B_{\rm offset}$, α and A as the fit parameters. We can fit multiple transitions simultaneously, as in Fig. 3, or fit a single transition, as in Fig. 4, using the `lsqnonlin` function provided by the MATLAB Optimization Toolbox. In both cases, the extracted α and $B_{\rm offset}$ are used to plot the data in terms of B_0 rather than $B_{\rm applied}$. The one standard deviation error bars quoted are calculated from $\sigma = \Delta\mathrm{C.I.}/4$, where ΔC.I. is the difference between the upper- and lower-value of the fitted 95% confidence intervals.

We find good agreement between the values of A and α determined by fitting simultaneously the parallel and perpendicular datasets and the values determined by fitting solely to the clock transition dataset. However, we observe a small difference between the fitted value of the offset field, which is $B_{\rm offset} = -28 \pm 4\,\mu\mathrm{T}$ for the former case and $B_{\rm offset} = -12.1 \pm 0.5\,\mu\mathrm{T}$ for the latter case. This difference between the offset fields is physically reasonable because the energy splitting is determined by $B_0 = |\alpha \boldsymbol{B}_{\rm coil} + \boldsymbol{B}_{\rm env}|$, where $\boldsymbol{B}_{\rm env}$ is a fixed environmental field set by, for example, the Earth's magnetic field. The fitted value of $B_{\rm offset}$ therefore depends on the relative orientation of the magnet field $\boldsymbol{B}_{\rm coil}$ and $\boldsymbol{B}_{\rm env}$, and hence differs between perpendicular and parallel mode operation.

[S1] C. P. Slichter, *Principles of Magnetic Resonance*, 3rd ed. (Springer-Verlag, 1990).